applied sciences

MDPI

Article

Kinematic Analysis and Performance Test of a 6-DOF Parallel Platform with Dense Ball Shafting as a Revolute Joint

Hasiaoqier Han [1], Yang Zhang [1,2], Hui Zhang [1,2], Chunyang Han [1], Ang Li [1] and Zhenbang Xu [1,2,*]

1 Changchun Institute of Optics, Fine Mechanics and Physics, Chinese Academy of Sciences, No. 3888, Dong Nanhu Road, Changchun 130033, China; hanhasiaoqier@yahoo.com (H.H.); zhangyang173@mails.ucas.ac.cn (Y.Z.); zhanghui171@mails.ucas.ac.cn (H.Z.); hanchunyang.312@163.com (C.H.); bcleon@126.com (A.L.)
2 Center of Materials Science and Optoelectronics Engineering, University of Chinese Academy of Sciences, Beijing 100049, China
* Correspondence: xuzhenbang@ciomp.ac.cn

Abstract: To meet the special requirements of the third mirror adjustment system for an optical telescope, a 6-*P*-RR-R-RR parallel platform using offset RR-joints is designed with high precision, a large load-to-size ratio and high stiffness. In order to improve the adjustment accuracy and the stiffness of the whole mechanism, each rotating joint in the subchain is designed as a zero-gap bead shaft system. When compared with a traditional Hooke joint, the offset RR joint has certain characteristics, including large carrying capacity and easy processing and adjustment, that effectively reduce the risk of interference with the joint during rotation and increase the working space of the entire machine. Because of the additional variables introduced by the offset joints, the kinematics problem becomes much more complicated. Regarding the *P*-RRRRR series subchain, the kinematics model is established using the Denavit–Hartenberg parameter method and then solved by the numerical iteration method. The stiffness of the parallel platform is analyzed and tested, including static and fundamental frequency. Motion performance testing of the parallel platform is performed.

Keywords: 6-*P*-RR-R-RR kinematic chain; kinematics; offset RR joint; stiffness

check for updates

Citation: Han, H.; Zhang, Y.; Zhang, H.; Han, C.; Li, A.; Xu, Z. Kinematic Analysis and Performance Test of a 6-DOF Parallel Platform with Dense Ball Shafting as a Revolute Joint. *Appl. Sci.* **2021**, *11*, 6268. https://doi.org/10.3390/app11146268

Academic Editor: Alberto Doria

Received: 17 May 2021
Accepted: 1 July 2021
Published: 7 July 2021

1. Introduction

When a large-caliber telescope is in orbit, the relative positional relationships between the optical components may change because of factors including shock vibration, gravity release, temperature changes, and air pressure changes. Changes in the relative pose between the primary scope, the secondary mirror, and the third mirror of the telescope have a major influence on the imaging quality of the optical system, so it is necessary to use a high-precision adjustment mechanism to adjust this pose. The six degrees-of-freedom (6-DOF) configuration is commonly used in parallel adjustment mechanisms because of its high stiffness; examples include the 6-SPS configuration [1,2], the 6-UCU configuration [3], the 6-UPS configuration [4], and the 6-RUS configuration [5,6]. When compared with the 6-DOF configuration, configurations with fewer DOFs are easier to control and operate and configurations that have attracted the attention of many researchers include the 3-DOF configurations 3-PPS [7], 3-RPS [8], 2PRU-UPR [9], 3-TPT [10], 3-UPU [11], the 4-DOF configurations 4-PRRRR [12], 2-RPU and 2-SPS [13], and the 5-DOF configurations 3-PPUR [14] and 4SPU+UPU [15]. The 6-DOF parallel platform under study in this paper is used to adjust the third mirror poses of large-diameter telescopes precisely. To meet the requirements for high precision, a large load-size ratio and high stiffness, a 6-*P*-RR-R-RR configuration is used for the platform. To perform preliminary ground verification and meet the practical application needs, research is carried out on the kinematics solution and the stiffness and motion performances.

The parallel mechanism was first used in aircraft tire tests [16]. Since then, parallel mechanisms have been used widely in many fields. These practical applications include:

motion simulators [17,18], parallel machine tools [19,20], a 6-DOF micro vibration simulator [21], and a space optical load isolation system [22]. Most telescope secondary mirror or third mirror adjustment systems use parallel mechanisms, including the Visible and Infrared Survey Telescope for Astronomy (VISTA) secondary mirror system [23], and the Very Large Telescope Survey Telescope (VST) secondary mirror system [24]. In recent years, parallel mechanisms have also increasingly been used in surgical procedures, including spinal surgery [25] and ophthalmic surgery [26].

The kinematics analysis of the parallel mechanism does not involve forces or moments, nor does it study the forces or moments generated by the motion. The analysis mainly studies the mapping relationship between the position, the velocity and the acceleration of the mobile platform and the active joint input of the leg that produces the motion; among these factors, the position research is the main basis. The kinematics problems of parallel mechanisms can be divided into inverse kinematics and forward kinematics, and the forward kinematics problem is much more complex than that of inverse kinematics.

Parallel mechanisms for common configurations, such as 6-SPS, 6-UCU, and 6-SPU, have simple structures and their inverse kinematics have analytical solutions [27–29]. However, with the continuing development of parallel mechanisms, a variety of parallel platforms with new structural forms have emerged and inverse kinematics solutions cannot be obtained for these platforms by analytical methods. There is a specific offset distance between the two spatially perpendicular rotating axes of the offset RR joint, and when additional offset variables are introduced, the kinematics of a parallel mechanism with an offset joint becomes quite complex. Ji and Wu [30] studied an offset 3-UPU parallel mechanism with three translational degrees of freedom, established the inverse kinematics and forward kinematics equations for this mechanism, and demonstrated that the mechanism has two inverse kinematics solutions. Two passive offset Hooke joints were used at both ends of each leg, and the two rotational axes of the offset joints were perpendicular to each other. Hu and Lu [31] studied a 3-RRPRR parallel mechanism with two passively offset RR joints at each end of its legs. The two axes of rotation of the offset joints intersected at one point and lay perpendicular to each other with an offset. The lengths of the three legs were varied using an active moving pair. Dalvand et al. [32–34] studied a new 6-RRCRR parallel platform that used biased joints and established a kinematics model for this platform. However, because of the existence of joint offset, the inverse kinematics solution could not be determined using analytical methods. The Newton-Raphson numerical iteration method is used to solve kinematics problems. To improve the motion accuracy, working space, and stiffness characteristics of parallel mechanisms, the German researchers Großmann and Kauschinger [35] studied three different forms of offset joints and discussed the feasibility of using these joints to replace traditional Hooke joints. Kinematics models of the traditional 6-UCU Hexapod platform and the 6-UCRR platform with offset joints were established and their kinematics solution processes were compared.

The 6-*P*-RR-R-RR parallel platform studied takes stiffness as an important performance, and both longitudinal stiffness and lateral stiffness should be taken into account. In this parallel platform, an offset RR joint replaces the traditional Hook joint. When compared with a traditional Hooke joint, the offset RR joint [35,36] has characteristics including large carrying capacity and easy processing and adjustment, effectively reducing the risk of interference with the joint during rotation and increasing the working space of the entire machine. This offset joint structure is beneficial in improving the stiffness of the entire platform. All revolute joints in the subchain use a zero-gap dense ball shaft to replace the traditional bearing and the installation datum is designed to improve the accuracy and the stiffness of the kinematic chain. The effectiveness of the proposed design in improving the stiffness is verified via experiments and simulation analyses. There is an offset between the two axes of rotation of the offset joint and additional variables are introduced, thus making the platform kinematics more complex. To solve the complex kinematics problem of the platform effectively, an inverse kinematics and forward kinematics model of the 6-*P*-RR-R-RR parallel platform was established using the Denavit–Hartenberg

(D-H) parameter method for series mechanisms. The kinematics problem was solved using numerical iterative methods and the correctness of the kinematics model was verified through simulations.

The remainder of this paper is divided into four sections. The second section mainly introduces the structural design of the parallel platform, including the platform composition and the revolute joint design. The third section mainly studies the method used to establish the kinematics model of the platform, along with the inverse kinematics and forward kinematics solutions. The fourth section mainly describes the experimental research, including the static and dynamic stiffness tests and the motion performance testing. Finally, the fifth section provides an overall summary of the research work.

2. Structural Design of the Platform

2.1. Composition of the Platform

The parallel platform designed in this paper consists of a mobile platform, a base platform, six legs, six leg drive components, and twelve offset joints, as shown in Figure 1. The parallel platform has a 6-*P*-RR-R-RR kinematic chain. According to the Kutzbach-Grübuler formula for the degrees of freedom of spatial mechanisms, the parallel platform has six degrees of freedom.

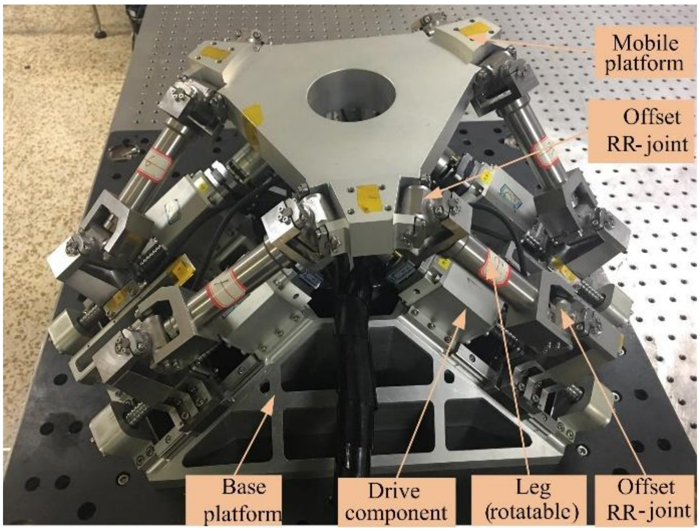

Figure 1. Configuration and structural components of the parallel platform.

To improve the motion resolution and accuracy of the proposed platform, a stepping motor was used to drive a high-precision ball screw through the zero-backlash harmonic reducer, and a grating ruler reading head with resolution of 50 nm was used as a feedback element to realize closed-loop control of the leg driving ramp block. Clearance elimination processing was performed for each link.

The platform structure has small axial dimensions and large lateral stiffness characteristics. The conventional leg telescopic driving method was changed to a slider driving the lower joint, and the leg driving assembly was fixed directly to the base platform. The base platform was provided with a mounting surface for the driving component, which was set at an angle of 30° with respect to the horizontal plane, which is beneficial for the improvement of the movement stroke of the entire platform. This design also reduces the weight and the inertia of the entire collection of moving parts, thereby helping to reduce the number of harmful disturbances of the entire satellite platform caused by orbital motion.

2.2. Dense Bead Shaft Joint

2.2.1. Design of Joint and Leg

The parallel platform uses an RR-R-RR series structure for each leg's kinematic chain. Each subchain contains two joints and one leg, and thus, includes five degrees of freedom of movement. Parts with freedom of movement, such as the joints and the legs, are very important to the overall stiffness of the platform, and the accuracy of the platform's motion is mainly dependent on the gap sizes of the moving parts. Therefore, the joint and leg designs are critical to the accuracy and the stiffness of the machine. The joint uses two rows of high-precision large-diameter dense-bead steel ball arrays symmetrical on both ends of the joint shaft to replace the pair of bearings, which can increase the diameter of the joint shaft and effectively reduce the offset amount and overall size of the offset joint. Pre-tighten the steel balls quantitatively through nuts and end caps to reduce axial clearance. Design the installation benchmark at one end of each joint shaft. The above-mentioned design of the joint greatly improves the bearing capacity, the motion precision, and stiffness of the joint. The prototype and explosion diagram of the joint are shown in Figure 2.

Figure 2. Prototype and explosion diagram of joint.

To allow it to adapt to the structural form of the joint and the mounting and positioning methods, the leg structure is designed as shown in Figure 3. In addition, to provide further improvements in the bearing capacity, the stiffness and the motion accuracy of the legs, high-precision steel balls are used, and the diameters of the steel balls used in the dense ball steel arrays arranged at both ends of the bearing are increased.

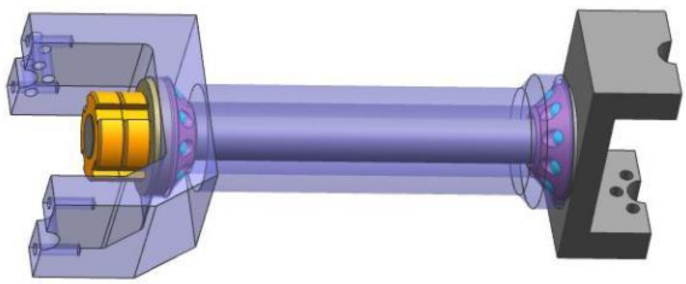

Figure 3. 3D model of the leg.

To improve the stiffness of both the joints and the legs, the materials and the heat treatment method are selected, and the material hardness is controlled strictly. At the same time, the axial pre-tightening forces of the joints and the legs are controlled quantitatively to ensure that the pre-tightening states of the twelve joints and six legs are both consistent and interchangeable. In addition, to improve the movement accuracy of the entire machine, the joint installation process has been improved and an installation benchmark has been defined for the new joint. The gap control assembly method that was used for the original joint end face and the joint seat has been changed to a direct contact installation process. This process greatly improves the installation accuracy of the joints and the mobile platform, while the legs and the slider make the physical platform configuration parameters closer to the theoretical configuration parameters, thus improving the motion accuracy of the entire platform.

2.2.2. Stiffness Chain Analysis

By analyzing the platform's stiffness chain, the components that affect the platform stiffness are determined and the main links that affect the stiffness of the entire machine are also determined using the finite element simulation method. When a load is installed on the mobile platform, the force transfer block diagram is as shown in Figure 4. The upper offset shaft 1 refers to the upper offset joint shaft connected to the mobile platform, and the upper offset shaft 2 refers to the upper offset joint shaft connected to the leg. The lower offset shaft 1 refers to the lower offset joint shaft connected to the leg, and the lower offset shaft 2 refers to the lower offset joint shaft connected to the slider. The load force is initially transmitted to the slider through the mobile platform and is then transferred from the slider to the base platform via two transmission routes. The order of force transmission in the joint is from the first joint axis → steel ball array → joint seat → second joint axis. The force transmission route in the leg is from the inner shaft of the leg → the steel ball array → the outer seat of the leg.

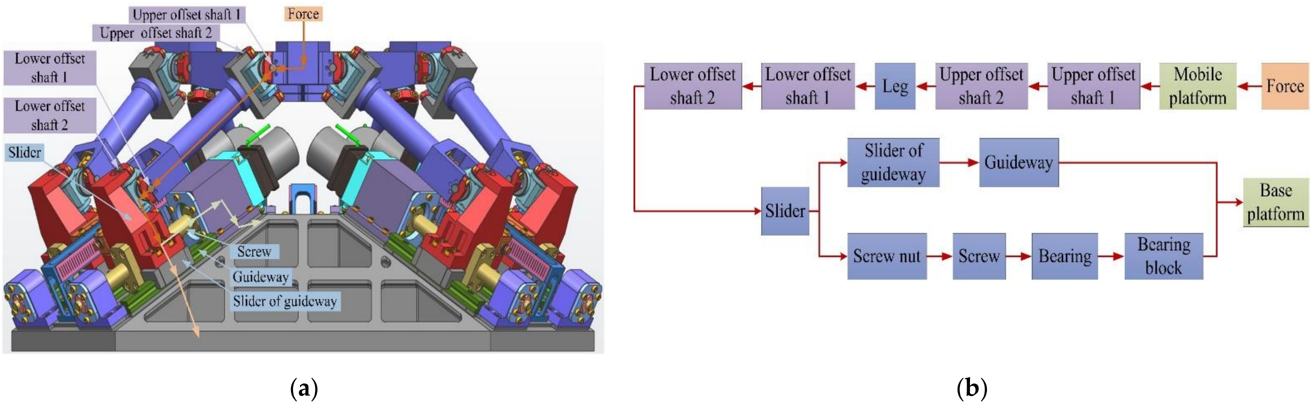

Figure 4. Force transfer analysis: (**a**) Transfer chain of force; (**b**) Block diagram of force transfer process.

To locate the main links among the many factors that affect the overall stiffness characteristics of the entire machine, a mechanical simulation analysis method in which the elastic modulus of each link can be changed is used to perform a comparison study. When the elastic modulus of a component is changed, the ratio of the fundamental frequency of the entire machine to the fundamental frequency of the entire machine at the elastic modulus $\varepsilon = 1$ can be obtained. Then, the contributions of each component to the stiffness of the entire machine were obtained, as shown in Figure 5. The term ε refers to the ratio between the modulus of elasticity of a component and its reference modulus of elasticity. According to the preliminary selection of materials for each component, the fundamental frequency (reference fundamental frequency) of the entire machine is calculated, and the elastic modulus of each component is recorded as the reference elastic modulus. The joint shaft stiffness has the greatest influence on the stiffness of the entire machine. Therefore, the joint stiffness is an important indicator in the design process. In addition, for parts with freedoms of motion, such as the joints and legs, improvements should be made in terms of material selection, heat treatment, the machining processes, and the assembly process to improve both the stiffness and the motion accuracy of important components.

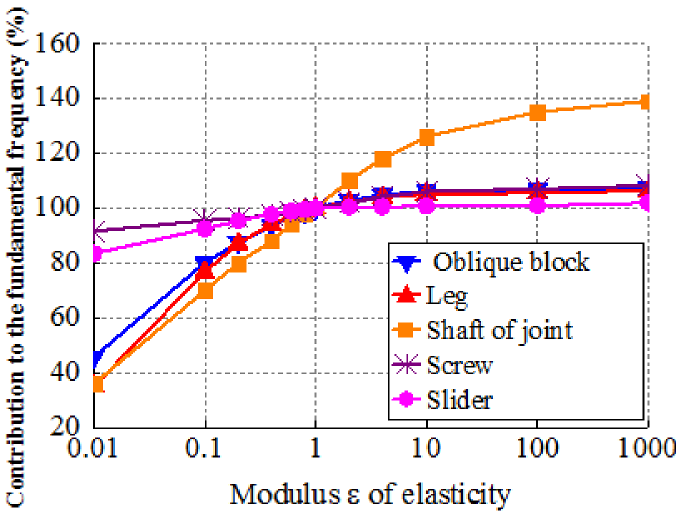

Figure 5. Effects of each component on the stiffness of the entire mechanism.

3. Kinematics Analysis

The kinematics modeling and analysis of the 6-*P*-RR-R-RR parallel platform with the offset joint are carried out in this section. The main contents of this section are the kinematic analysis and the simulation verification. The D-H parameter method for series mechanisms is used to establish the inverse kinematics model of the proposed platform, and numerical iteration methods are used to solve the inverse kinematics problem. The forward kinematics model of the platform is then also established and solved. Furthermore, ADAMS and MATLAB software are used to verify the correctness and the validity of the kinematic modeling and the solution processes.

3.1. Platform Configuration Parameters

The mobile platform is connected to the base platform through the legs and the joints at both ends of the legs, where these legs have the degree of freedom of rotation. The joint adopted is an offset joint, in which the rotation center lines of the two rotation pairs lie perpendicular to each other but do not intersect, and they also have a specific offset that allows them to form an RR joint, as shown in Figure 6a,b. The lower joint is connected to the sliding block, which moves in a straight line along double guide rails that are arranged at an angle of 30° with respect to the horizontal plane. Figure 6c shows the composition of the P-RR-R-RR leg drive chain of the parallel platform.

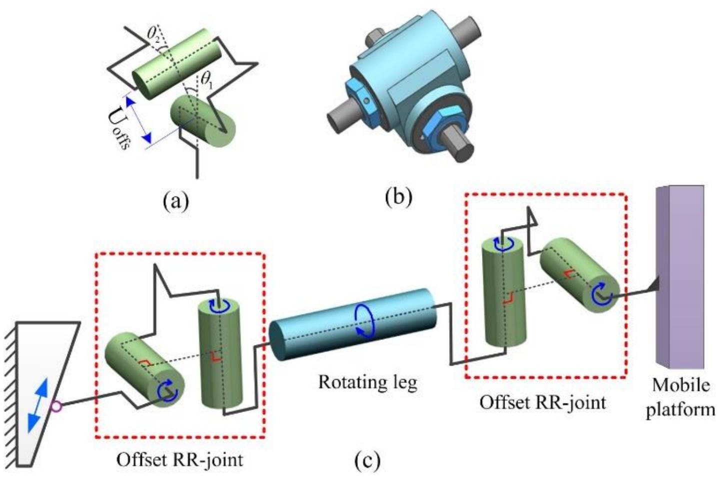

Figure 6. *P*-RR-R-RR kinematic chain: (**a**) Schematic diagram of offset RR-joint; (**b**) 3D model of offset RR-joint; (**c**) *P*-RR-R-RR kinematic chain composition.

To describe the motion of the mobile platform, a global coordinate system denoted by $O_B - X_B Y_B Z_B$ is established at the center O_B of the base of the base platform. A local coordinate system denoted by $O_P - X_P Y_P Z_P$ is established at the center O_P of the upper surface of the mobile platform. The six joint points P_i (i = 1, . . . ,6) of the mobile platform form a 120° symmetrical hexagon, and the circle formed by P_i has a center denoted by $O_P{}'$ and a radius R_P, and the center angle θ_P of P_i is distributed. When the mobile platform is at the zero position, the six lower joint points denoted by B_i (i = 1, . . . ,6) also form a symmetrical hexagon, and the circle formed by B_i has a center denoted by $O_B{}'$, the radius is R_B, and the center angle θ_B of B_i is distributed. The distance between the center $O_P{}'$ and the center O_P of the top surface of the mobile platform is denoted by H_P. The distance between the center $O_B{}'$ and the center O_B of the bottom of the base platform is denoted by H_B. When the mobile platform is at the zero position, the distance between the circle center $O_P{}'$ and the circle center $O_B{}'$ is H. The offset amounts of the upper and lower joints are expressed as U_P and U_B, respectively. The above coordinate systems and parameters are shown in Figures 7 and 8. The parallel platform configuration parameters are presented in Table 1.

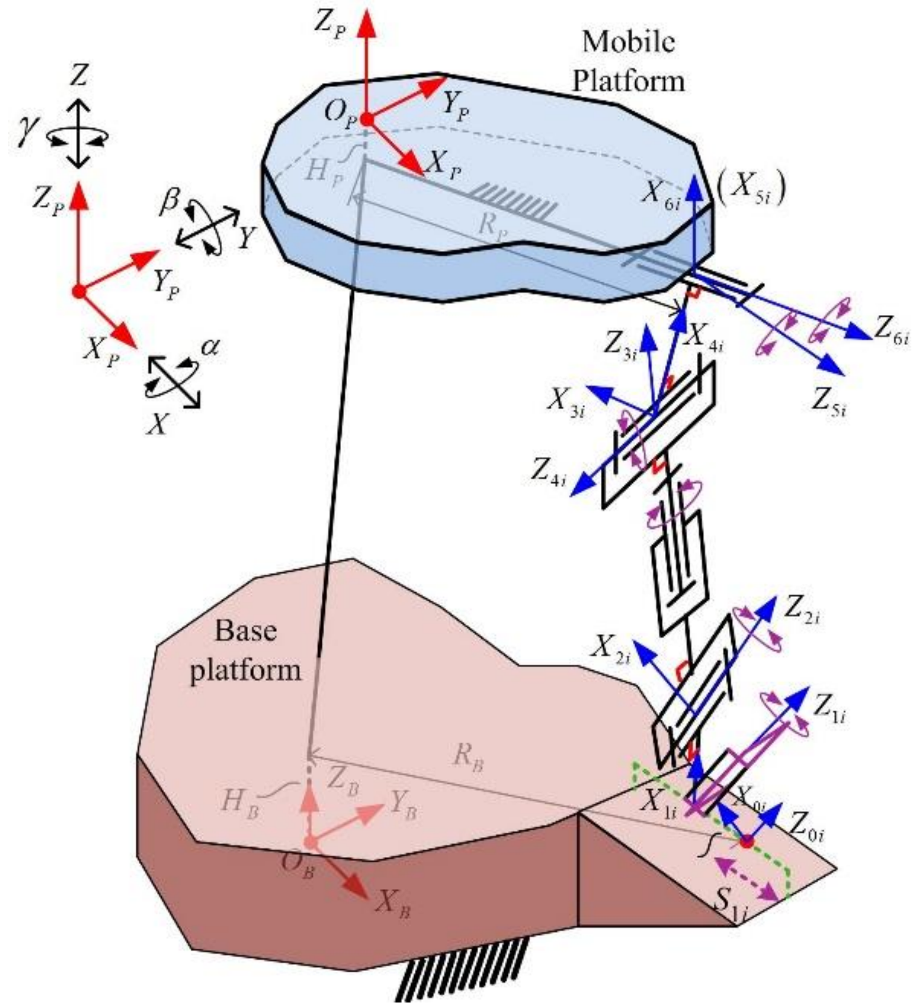

Figure 7. Definition of body coordinate systems for the platform and the joints of the i_{th} leg.

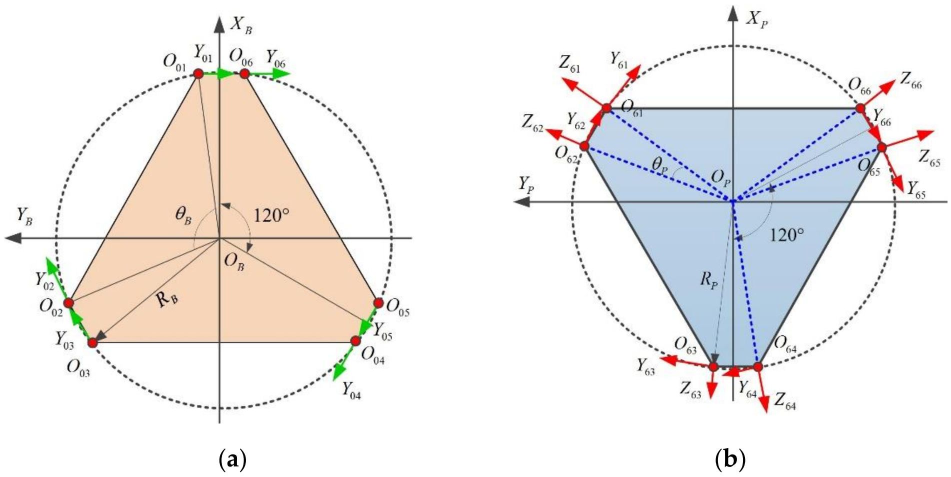

Figure 8. Layouts of local coordinate systems: (**a**) At the base platform; (**b**) At the mobile platform.

Table 1. Parallel platform configuration parameters.

Parameter	Value
R_P	0.13 m
R_B	0.222 m
θ_P	30°
θ_B	90°
U_P	0.01 m
U_B	0.01 m
H	0.1 m
H_P	0.066 m
H_B	0.128 m

The spatial pose of the mobile platform in the global coordinate system $O_B - X_B Y_B Z_B$ is determined using the six-dimensional vector $[X,\ Y,\ Z,\ \alpha,\ \beta,\ \gamma]$. Among these dimensions, $[X,\ Y,\ Z]$ and $[\alpha,\ \beta,\ \gamma]$ indicate the position and the orientation of the mobile platform, respectively. The transfer matrix of the moving coordinate system $O_P - X_P Y_P Z_P$, when transformed into the global coordinate system $O_B - X_B Y_B Z_B$ according to the RPY rules, can be expressed as follows:

$$ {}^{O_B}\boldsymbol{T}_{O_P} = \begin{bmatrix} c\beta c\gamma & -c\beta s\gamma & s\beta & X \\ c\alpha s\gamma + s\alpha s\beta c\gamma & c\alpha c\gamma - s\alpha s\beta s\gamma & -s\alpha c\beta & Y \\ s\alpha s\gamma - c\alpha s\beta c\gamma & s\alpha c\gamma + c\alpha s\beta s\gamma & c\alpha c\beta & Z \\ 0 & 0 & 0 & 1 \end{bmatrix} \tag{1} $$

where c ( ) = cos ( ) and s ( ) = sin ( ).

3.2. Inverse Kinematics

The inverse kinematics aims to find the drive displacements of driving parts given the pose of the mobile platform. As shown in Figure 7, based on the global coordinate system, we established a base platform local coordinate system $O_{0i} - X_{0i} Y_{0i} Z_{0i}$ (i = 1, . . . , 6), where the point O_{0i} (coincidence point B_i at the zero position) is the origin. Based on the mobile platform's local coordinate system, the mobile platform local coordinate system $O_{6i} - X_{6i} Y_{6i} Z_{6i}$ (i = 1, . . . , 6) is established with the point O_{6i} (coincident with point P_i) as its origin. Because of the presence of the offset joint, it is necessary to create five additional local coordinate systems on each leg, which are denoted by systems $O_{1i} - X_{1i} Y_{1i} Z_{1i}$ (i = 1, . . . , 6) to $O_{5i} - X_{5i} Y_{5i} Z_{5i}$ (i = 1, . . . , 6).

Each leg of the proposed parallel platform can be equivalent to the P-RR-R-RR series mechanism. According to the D-H parameter theory used for series robots, the D-H parameter of the i_{th} leg can be obtained as shown in Table 2. Here, S_{1i} represents the displacement of the lower joint point B_i along the inclined plane. Based on the D-H parameter method, the kinematics transformation matrix for the i_{th} leg kinematic chain of the parallel platform can be derived as:

$$^{j}\boldsymbol{T}_{6(i)} = \boldsymbol{A}_{j+1(i)} \cdots \boldsymbol{A}_{6(i)} \ (j = 0,\ 1, \cdots, 5) \tag{2}$$

where $\boldsymbol{A}_{j(i)}$ is the transformation matrix between two adjacent coordinate systems.

Table 2. D-H parameters of the kinematic chain of the i_{th} leg.

Link *j*	$\boldsymbol{\theta_{ji}}$	$\boldsymbol{d_{ji}}$	$\boldsymbol{a_{(j-1)i}}$	$\boldsymbol{\alpha_{(j-1)i}}$
1	θ_{2i}	$S_{1i} \cdot \sin\phi$	$S_{1i} \cdot \cos\phi$	0
2	θ_{3i}	0	U_B	$-\pi/2$
3	θ_{4i}	L	0	$-\pi/2$
4	θ_{5i}	0	0	$\pi/2$
5	θ_{6i}	0	U_P	$\pi/2$
6	0	0	0	$\pm\lambda$

The parameters $L = 0.151854915568$, $\phi = 9.223°$, and $\lambda = 29.2871793765 * \pi/180$.

The distribution diagrams of the local coordinate systems that were defined on the base and mobile platforms are shown in Figure 8. The position of the origin O_{0i} of the local coordinate system in $O_B - X_B Y_B Z_B$ is expressed as:

$$^{O_B}\boldsymbol{O}_{0i} = \begin{bmatrix} R_B \cdot c\theta_{O_{0i}} & R_B \cdot s\theta_{O_{0i}} & H_B \end{bmatrix}^T \tag{3}$$

The position of the origin O_{6i} of the local coordinate system in $O_P - X_P Y_P Z_P$ is then expressed as:

$$^{O_P}\boldsymbol{O}_{6i} = \begin{bmatrix} R_P \cdot c\theta_{O_{6i}} & R_P \cdot s\theta_{O_{6i}} & -H_P \end{bmatrix}^T \tag{4}$$

The static coordinate system $O_B - X_B Y_B Z_B$ first rotates at the angle $\theta_{Z_B(i)}$ around the axis Z_B and then rotates at the angle $\theta_{Y'_B(i)}$ around the new axis Y'_B so that the newly obtained coordinate system has the same orientation as $O_{0i} - X_{0i} Y_{0i} Z_{0i}$. In the coordinate system $O_{0i} - X_{0i} Y_{0i} Z_{0i}$, the definitions of X_{0i} and Z_{0i} are as shown in Figure 7, and the definitions of Y_{0i} are as shown in Figure 8. The expression for the transfer matrix $^{O_B}\boldsymbol{T}_{O_{0i}}$ of $O_{0i} - X_{0i} Y_{0i} Z_{0i}$ to $O_B - X_B Y_B Z_B$ is given as follows:

$$^{O_B}\boldsymbol{T}_{O_{0i}} = \begin{bmatrix} ^{O_B}\boldsymbol{R}_{O_{0i}} & ^{O_B}\boldsymbol{O}_{0i} \\ 0 & 1 \end{bmatrix} \tag{5}$$

where $^{O_B}\boldsymbol{R}_{O_{0i}}$ denotes the rotation matrix of $O_B - X_B Y_B Z_B$ to $O''_B - X''_B Y''_B Z''_B$.

Similarly, the transfer matrix $^{O_P}\boldsymbol{T}_{O_{6i}}$ from $O_{6i} - X_{6i} Y_{6i} Z_{6i}$ to $O_P - X_P Y_P Z_P$ is expressed as follows:

$$^{O_P}\boldsymbol{T}_{O_{6i}} = \begin{bmatrix} ^{O_P}\boldsymbol{R}_{O_{6i}} & ^{O_P}\boldsymbol{O}_{6i} \\ 0 & 1 \end{bmatrix} \tag{6}$$

The transformation matrices $^{O_B}\boldsymbol{T}_{O_{0i}}$ and $^{O_P}\boldsymbol{T}_{O_{6i}}$ are determined by the geometric parameters of the mobile and base platforms and the corresponding coordinate system definitions. Given the pose of the mobile platform in $O_B - X_B Y_B Z_B$, the transformation matrix $^{O_{0i}}\boldsymbol{T}_{O_{6i}}$ can also be determined, and the following relationship exists:

$$^{O_{0i}}\boldsymbol{T}_{O_{6i}} = \left(^{O_B}\boldsymbol{T}_{O_{0i}}\right)^{-1} \cdot {}^{O_B}\boldsymbol{T}_{O_P} \cdot {}^{O_P}\boldsymbol{T}_{O_{6i}} \tag{7}$$

Each element of the transformation matrix $^{O_{0i}}\boldsymbol{T}_{O_{6i}}$ is known and $^{0}\boldsymbol{T}_{6(i)} = {}^{O_{0i}}\boldsymbol{T}_{O_{6i}}$. Therefore:

$$\boldsymbol{T}_i = {}^{0}\boldsymbol{T}_{6(i)} - {}^{O_{0i}}\boldsymbol{T}_{O_{6i}} = 0 \tag{8}$$

The inverse kinematics problem involves solution of six nonlinear equations, where each leg corresponds to a nonlinear equation group, and the corresponding nonlinear equations of the i_{th} leg contain the unknown parameters S_{1i}, θ_{2i}, θ_{3i}, θ_{4i}, θ_{5i}, and θ_{6i}. The six matrix elements in the matrix $\boldsymbol{T}_i$ are selected to form a system of nonlinear equations that contains six equations that correspond to the i_{th} leg. The expression for these nonlinear equations is given as follows:

$$\begin{cases} \Phi_{1i}(S_{1i}, \theta_{2i}, \theta_{3i}, \theta_{4i}, \theta_{5i}, \theta_{6i}) = \boldsymbol{T}_i(2,1) = 0 \\ \Phi_{2i}(S_{1i}, \theta_{2i}, \theta_{3i}, \theta_{4i}, \theta_{5i}, \theta_{6i}) = \boldsymbol{T}_i(2,2) = 0 \\ \Phi_{3i}(S_{1i}, \theta_{2i}, \theta_{3i}, \theta_{4i}, \theta_{5i}, \theta_{6i}) = \boldsymbol{T}_i(1,3) = 0 \\ \Phi_{4i}(S_{1i}, \theta_{2i}, \theta_{3i}, \theta_{4i}, \theta_{5i}, \theta_{6i}) = \boldsymbol{T}_i(2,3) = 0 \\ \Phi_{5i}(S_{1i}, \theta_{2i}, \theta_{3i}, \theta_{4i}, \theta_{5i}, \theta_{6i}) = \boldsymbol{T}_i(1,4) = 0 \\ \Phi_{6i}(S_{1i}, \theta_{2i}, \theta_{3i}, \theta_{4i}, \theta_{5i}, \theta_{6i}) = \boldsymbol{T}_i(3,4) = 0 \end{cases} \tag{9}$$

The Newton-Raphson numerical iterative method is used to solve the nonlinear equations given as Equation (9). Solutions can be derived for the unknown parameters S_{1i}, θ_{2i}, θ_{3i}, θ_{4i}, θ_{5i}, and θ_{6i} using the following iterative format:

$$\begin{bmatrix} S_{1i} \\ \theta_{2i} \\ \theta_{3i} \\ \theta_{4i} \\ \theta_{5i} \\ \theta_{6i} \end{bmatrix}_{(n+1)} = \begin{bmatrix} S_{1i} \\ \theta_{2i} \\ \theta_{3i} \\ \theta_{4i} \\ \theta_{5i} \\ \theta_{6i} \end{bmatrix}_{(n)} - \begin{bmatrix} \frac{\partial\Phi_{1i}}{\partial S_{1i}} \frac{\partial\Phi_{1i}}{\partial\theta_{2i}} \cdots \frac{\partial\Phi_{1i}}{\partial\theta_{6i}} \\ \vdots \\ \frac{\partial\Phi_{6i}}{\partial S_{1i}} \frac{\partial\Phi_{6i}}{\partial\theta_{2i}} \cdots \frac{\partial\Phi_{6i}}{\partial\theta_{6i}} \end{bmatrix}_{(n)}^{-1} \cdot \begin{bmatrix} \Phi_{1i} \\ \Phi_{2i} \\ \Phi_{3i} \\ \Phi_{4i} \\ \Phi_{5i} \\ \Phi_{6i} \end{bmatrix}_{(n)} \tag{10}$$

In addition to establishing an iterative format to solve these nonlinear equations, the initial value of the required solution variable is also given. The initial values${S_{1i}}^{(0)}$, ${\theta_{2i}}^{(0)}$, ${\theta_{3i}}^{(0)}$, ${\theta_{4i}}^{(0)}$, ${\theta_{5i}}^{(0)}$, and ${\theta_{6i}}^{(0)}$ can be variables of the i_{th} leg when the mobile platform is at the zero position. The flow chart for the iterative solution to the inverse kinematics of the platform when using the D-H parameter method is shown in Figure 9.

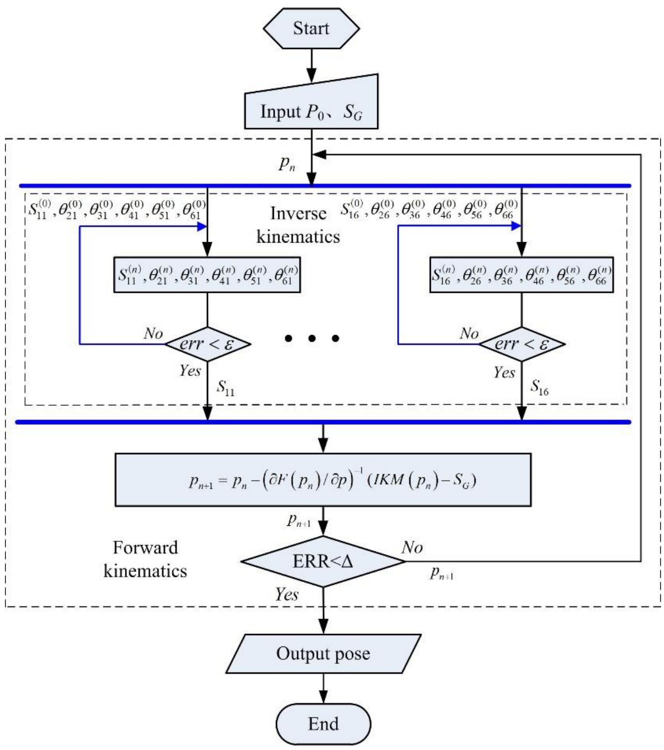

Figure 9. Solution procedure for the forward kinematics.

3.3. Forward Kinematics

3.3.1. Modeling and Solution of Forward Kinematics

The problem with determining the forward solution for the platform is that the displacements of the six leg-driven oblique blocks must be known to solve for the pose of the platform. The forward kinematics problem of the parallel mechanism has not yet found an analytical solution and it is difficult to solve using the closed-loop vector method. The solution process involves a problem composed of nonlinear equations, which are usually solved via numerical methods. After the displacements of the six leg-driven oblique blocks are given, the equations for the relationship between the displacements of the oblique block and the pose of the mobile platform are established using the D-H method.

For a given slider displacement $S_G = [S_{1G}, S_{2G}, \ldots, S_{6G}]^T$, the function $F(p)$ is defined as follows:

$$F(p) = IKM(p) - S_G \tag{11}$$

$IKM(p)$ is the inverse kinematic solution $[S_1, S_2, \ldots, S_6]^T$, which corresponds to the platform pose $p = [X, Y, Z, \alpha, \beta, \gamma]^T$. The vector $[\alpha\ \beta\ \gamma]$ indicates the orientation of the mobile platform. According to RPY rules, the mobile platform rotates α angle around X_B axis, β angle around Y_B axis, and γ angle around Z_B axis. The Newton-Raphson numerical iterative method can be used to solve Equation (11), so the following numerical iteration format is obtained:

$$p_{n+1} = p_n - (\partial F(p_n)/\partial p)^{-1}[IKM(p_n) - S_G] \tag{12}$$

where:

$$\frac{\partial F}{\partial p} = \begin{bmatrix} \frac{\partial S_1}{\partial X} & \frac{\partial S_1}{\partial Y} & \frac{\partial S_1}{\partial Z} & \frac{\partial S_1}{\partial \alpha} & \frac{\partial S_1}{\partial \beta} & \frac{\partial S_1}{\partial \gamma} \\ \vdots & \vdots & \vdots & \vdots & \vdots & \vdots \\ \frac{\partial S_6}{\partial X} & \frac{\partial S_6}{\partial Y} & \frac{\partial S_6}{\partial Z} & \frac{\partial S_6}{\partial \alpha} & \frac{\partial S_6}{\partial \beta} & \frac{\partial S_6}{\partial \gamma} \end{bmatrix} \tag{13}$$

By selecting the initial value appropriately, the algorithm can converge quickly to the theoretical pose. After the initial value p_0 is given, the iterative format given in Equation (12) is used to perform the numerical iterative calculations. When the mobile platform pose is satisfied with $|p_{n+1} - p_n| \leq 1 \times 10^{-9}$, the iteration converges, and p_{n+1} is the final solution for the forward kinematics. The forward kinematics calculation flow when using the D-H parameter method is shown in Figure 9.

3.3.2. Verification of the Forward Kinematics Simulation

The correctness of the forward kinematics solution for the 6-*P*-RR-R-RR parallel platform is verified via a co-simulation using the ADAMS and MATLAB software. The pose and the motion trajectory of the mobile platform when solved using the MATLAB iterative algorithm are compared with the input pose and trajectory obtained from ADAMS and the pose error and the trajectory tracking error are obtained, thus verifying the correctness and the effectiveness of the forward kinematic algorithm. The correctness of the forward kinematics algorithm is verified by making the platform track a specific three-dimensional trajectory. The tracking curve is illustrated in Figure 10, and the mathematical expression for the curve is:

$$\begin{cases} x = 20 \sin \xi \cos \varsigma \\ y = 20 \sin \xi \sin \varsigma \\ z = 20 \cos \xi \end{cases} \text{and} \begin{cases} \xi = \pi t/10 \\ \varsigma = 20\pi t/10 \\ 0 \leq t \leq 10 \end{cases} \tag{14}$$

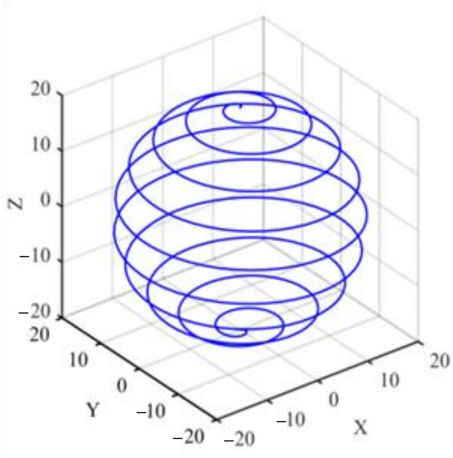

Figure 10. Spatial tracking path.

In ADAMS, the three attitude angles of the mobile platform are set to zero and the mobile platform is then controlled to move along the three-dimensional curve shown in Figure 10. The displacement corresponding to that of the six oblique driving blocks is extracted and is brought into the MATLAB iterative algorithm and used as the input to the forward kinematics. The pose errors of the mobile platform with respect to the motion time are solved using the iterative algorithm, as shown in Figure 11. Figure 11 shows that when the mobile platform tracks the required spatial curve motion with a specific attitude, the maximum positioning errors generated in the X, Y, and Z directions are 6.28 nm, 6.23 nm, and −45.14 nm, respectively, while the maximum rotational angle errors of α, β, and γ are −0.05894 μrad, 0.07117 μrad, and −0.03976 μrad, respectively, as determined by the Matlab numerical iterative algorithm, which verifies the correctness of the forward kinematics numerical iterative algorithm. Because the solution procedure for inverse kinematics is included in the solution procedure for forward kinematics, the verification of forward kinematics also shows the correctness of inverse kinematics.

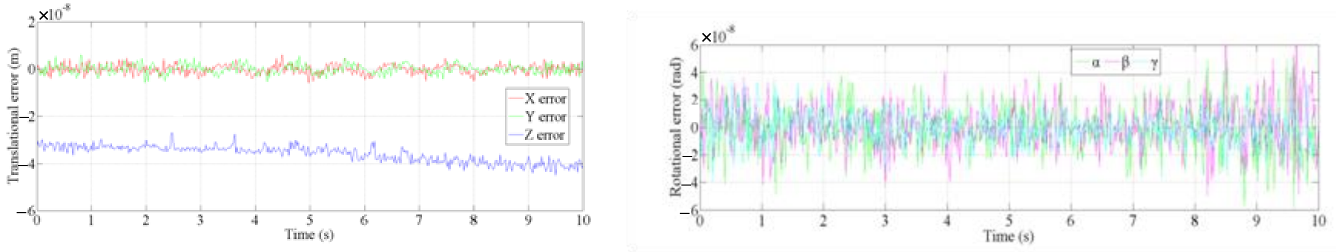

(**a**) (**b**)

Figure 11. Path tracking errors: (**a**) Position error; (**b**) Directional attitude angle error.

4. Research on Platform Performance Testing

4.1. Static Stiffness Testing

4.1.1. Stiffness Testing of the Subchain

The actual RR-R-RR subchain is pictured in Figure 12. The stiffness of the series subchain, which is composed of five revolute joints, makes the largest contribution to the overall stiffness of the machine according to Figure 5. Therefore, it is necessary to test the stiffness of the six series subchains. The stiffness test system is pictured in Figure 13 and is mainly composed of the fixed end of the subchain, a slide rail, the moving end of the subchain, a tension device, the grating length gauges and supporting parts, and a micro-displacement display instrument.

Figure 12. Prototype of RR-R-RR serial subchains.

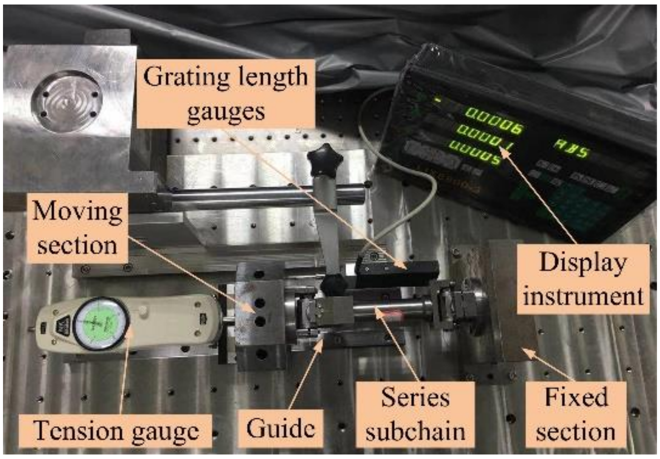

Figure 13. Stiffness testing setup for the RR-R-RR serial subchain.

The subchain is composed of a leg and two joints connected in series, and its axial stiffness is directly affected by the three components. Both legs and joints need to be preloaded quantitatively. By testing all the subchains, the stiffness range of the subchains can be clarified, and whether the pre-tightening force of the legs and joints has a large deviation can be determined, excluding the large stiffness deviations of individual subchains due to assembly or manufacturing errors. Using the stiffness test system shown in Figure 13, the axial deformations of the six subchains were measured under various tensile and extrusion loads, and the test points were then fitted linearly using the least squares method. The test points and the fitting lines are shown in Figure 14. As Figure 14 shows, the tensile stiffness values of the six subchains were in the 9.20 N/μm to 9.44 N/μm range, while the extrusion stiffness values were in 10.37 N/μm to 13.42 N/μm range. The deformation of the same subchain under an axial tensile load was greater than the deformation that occurred under an extrusion load. This phenomenon was mainly caused by the fact that under the axial tensile load, the main bearing parts were the connecting screws between the leg and the joint at both ends of the leg, rather than the joint shafts and the steel balls.

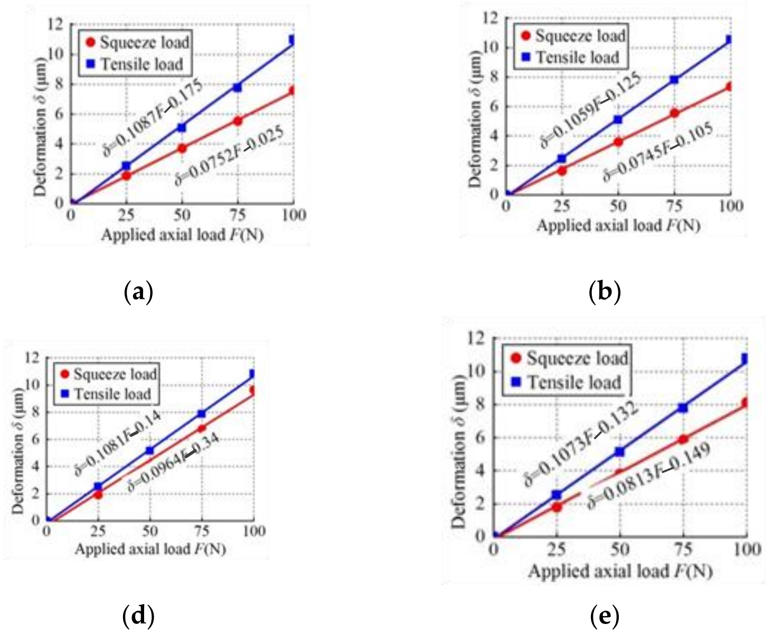

Figure 14. Results of stiffness testing of the RR-R-RR serial subchains: (**a**) Subchain 1; (**b**) Subchain 2; (**c**) Subchain 3; (**d**) Subchain 4; (**e**) Subchain 5; (**f**) Subchain 6.

4.1.2. Stiffness Testing of the Platform

To obtain the static stiffness index for the parallel platform, the static stiffness test was carried out on the actual platform at the zero position, as shown in Figure 15. The push force device was used to press the mobile platform along the X direction of the parallel platform and the grating length gauges were used to measure the small displacement that occurred at the other end of the mobile platform. Similarly, a standard weight was used to press the mobile platform along the Z direction of the parallel platform and the grating length gauges were then used to measure the small mobile platform displacement.

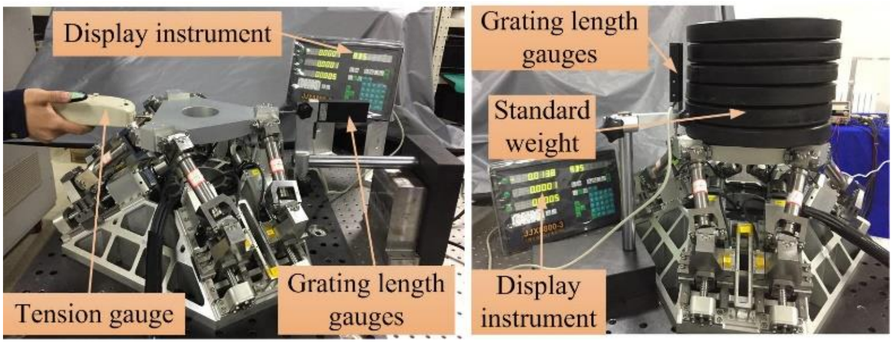

Figure 15. Static stiffness testing of the parallel platform.

In Figure 16, Z2 and X2 represent the stiffness data of the platform in the *Z*-axis and *X*-axis directions, respectively. The static stiffness of the parallel platform along the *Z*-axis and the *X*-axis were 21.71 N/μm and 7.84 N/μm, respectively, based on fitting of the test data.

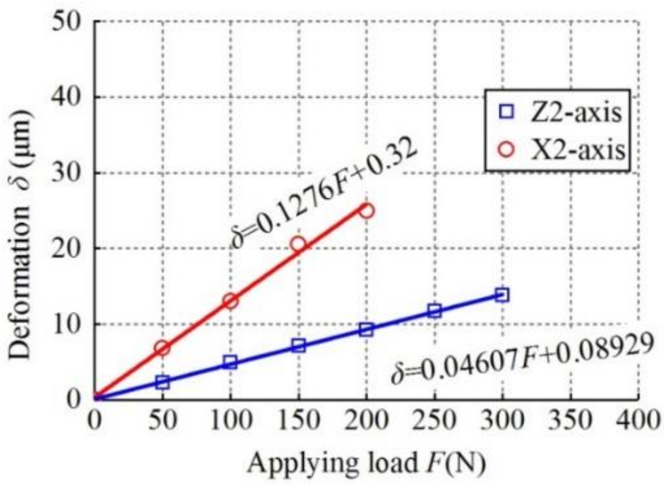

Figure 16. Static stiffness characteristics of the parallel platform.

4.2. Dynamic Stiffness Analysis and Testing of the Platform

According to the test results of the subchain tensile stiffness test, the finite element model of the subchain with equivalent stiffness was established, as shown in Figure 17a, and the finite element model of the whole mechanism was modified. The elastic modulus of the shaft corresponding to the axial stiffness was approximately 45 GPa. In order to simulate the vibration characteristics of the parallel mechanism installed with the third mirror, the finite element model used a 30 kg mass block to represent the load. In addition, due to the high stiffness of the base platform of the parallel adjustment mechanism, it did not contribute to the overall low-order natural frequency of the mechanism. In order to use the limited computing power to obtain a higher-precision fundamental frequency, the finite element model removes the base platform. The finite element simulation of the parallel adjustment mechanism is shown in Figure 17b,c. Through finite element simulation, it can be obtained that the fundamental frequency of the parallel adjustment mechanism was 94.5 Hz with the 30 kg load.

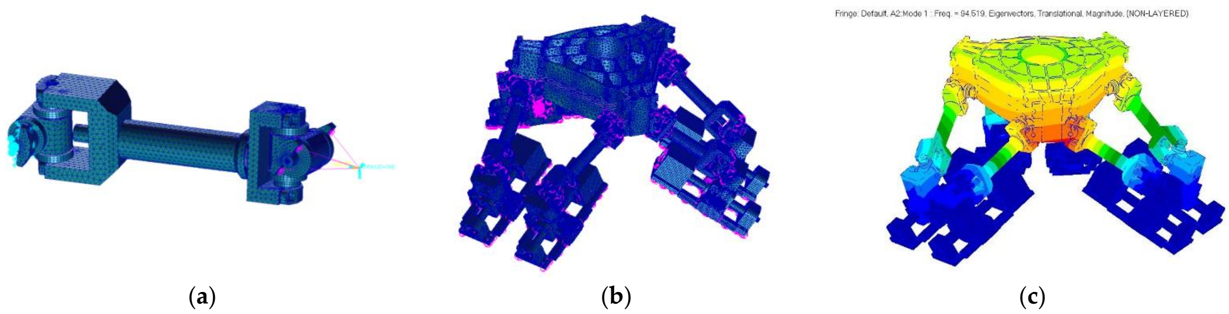

Figure 17. Finite element simulation of the third mirror adjustment mechanism: (**a**) Equivalent finite element model of subchain; (**b**) Finite element model of the whole mechanism; (**c**) Result of the finite element modal analysis.

To measure the natural frequency of the parallel platform at the zero position with a simulated load of 30 kg, an acceleration sensor was attached to the platform at the position with the highest vibration amplitude according to finite element simulation results and the platform is then tapped with a hammer. The natural frequency test system is pictured in Figure 18. The test system uploaded the vibration response data from the platform under test that were collected using the sensor to the computer and then generated the vibration response curve of the platform, as shown in Figure 19.

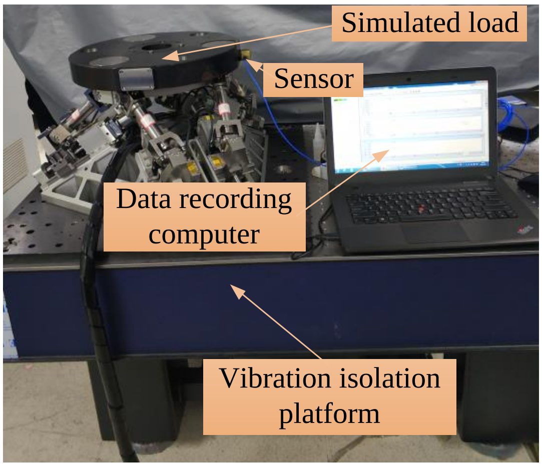

Figure 18. Natural frequency testing.

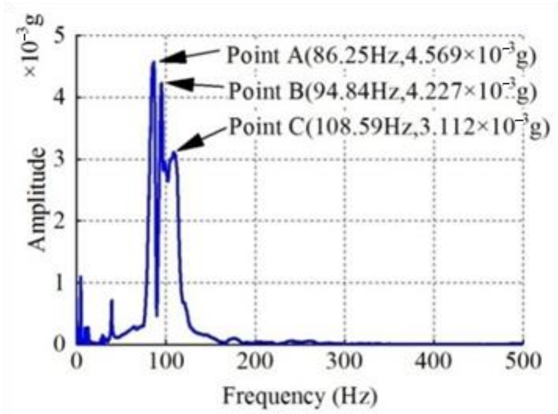

Figure 19. Vibration response curve.

Referring to the finite element simulation shown in Figure 17, the results of the analysis indicated that the natural frequency, which corresponds to the low-frequency peak at less than 50 Hz in Figure 19, was the natural frequency of the vibration isolation platform where the test system was placed, and the frequencies at the three peaks denoted by A, B, and C correspond to the natural frequencies of the entire platform (with a 30 kg load). The platform's fundamental frequency reached 86.25 Hz. The difference between the test data and the simulation data was mainly caused by the difference between the finite element model of the motion pair and its actual physical characteristics.

4.3. Initial Position Test

Because the accuracy of the platform zero position is critical to the motion accuracy of the whole machine, the zero position of the mobile platform must be calibrated accurately. The high-precision measurement arm was used to measure the characteristic line of the base platform, and this line was then used to determine the screw nut position of the leg accurately, thus ensuring positional consistency for the six driving sliders. The position of the driving slider ensured the theoretical position of the lower joint point. The zero calibration testing is pictured in Figure 20. With a measurement accuracy of 10 μm and a resolution of 1 μm, the Romer measuring arm ensured that the initial platform position was controlled to within 15 μm.

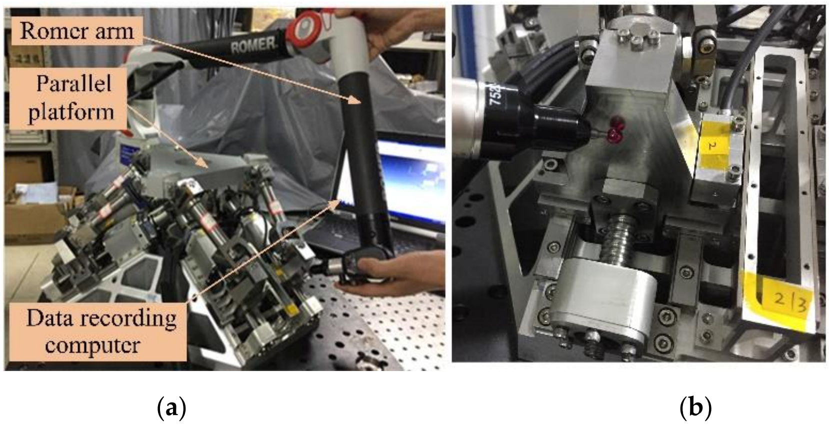

Figure 20. Calibration of the initial parallel platform position: (**a**) Overview; (**b**) Details.

4.4. Platform Motion Accuracy Testing

4.4.1. Composition and Principle of the Accuracy Testing System

In addition to platform stiffness testing, platform motion performance tests were also performed, including motion resolution and repeated positioning accuracy tests. The parallel platform test system was mainly composed of the test tooling, the simulation load, the parallel platform, the grating length gauges, and the display instruments, as pictured in Figure 21. The accuracy of each of the six degrees of freedom of the parallel platform was tested using the six grating length gauges in the test system.

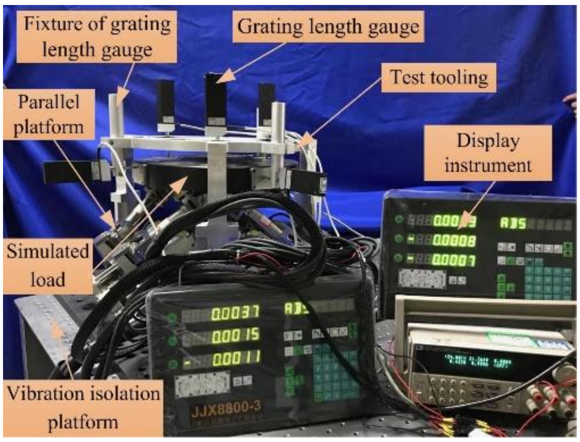

Figure 21. Test system configuration.

To improve the test accuracy, six standard blocks were processed using surface grinding treatments, and these standard blocks were then mounted on the simulated load to provide a contact surface for the test head of the grating length gauges, as shown in Figure 22. The defined coordinate system for the parallel platform and the grating length gauges layout are also shown in Figure 22. Grating length gauges no. 1 and no. 2 were used to test the translational displacements in the X direction and the Y direction, respectively. Grating length gauge no. 3 was used to test the Rz angular displacement. Grating length gauges no. 4, no. 5, and no. 6 were used to test the translational displacement in the Z direction and the Rx and Ry angular displacements, respectively.

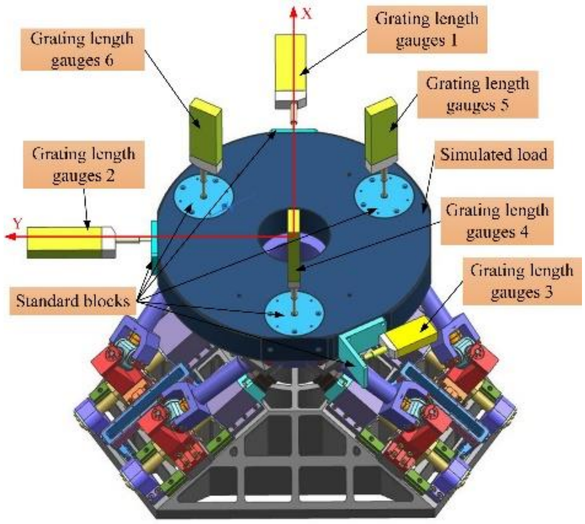

Figure 22. Definition of the coordinate system for the parallel platform and layout of the grating length gauges.

When the platform target pose was given, the displacement of the inclined block could be calculated using the inverse kinematics algorithm. Then, using the ball screw lead, the reduction ratio of the harmonic reducer, the step length of the stepping motor, and the motor driving steps corresponding to each slide displacement could be calculated. To improve the position control accuracy and stability, the electronic subdivision method was used to drive the motor. Open-loop control was adopted for each motion cycle. After the motion was complete, the controller evaluated the position error of the inclined block based on the value of the feedback from the grating ruler reading head that is installed on the inclined block. If a slider position error occurred because of the transmission clearance or a screw lead error, then the motor driving steps to be compensated were calculated, and the motor must then be driven to move into the next movement cycle. The previous step was repeated until the position error was less than a preset tolerance, which caused the motor to stop moving.

4.4.2. Repeated Positioning Accuracy Testing

The repeated positioning accuracy was measured using a fixed step size and multi-point cyclic measurements. The platform adjustment motion mainly involved a focusing motion along the Z-axis and pitch and yaw motions around the X- and Y-axes. Therefore, the accuracies of the Z-direction translation motion and the rotation motions in the Rx and Ry directions were the focus of this research. The testing of each step size was repeated three times.

Figure 23a,b show the three-cycle translational test curves along the Z direction in the ranges of $0\ \mu m \rightarrow 10\ \mu m \rightarrow 0\ \mu m \rightarrow -10\ \mu m \rightarrow 0\ \mu m$ with a $1\ \mu m$ step size and $0\ mm \rightarrow 5\ mm \rightarrow 0\ mm \rightarrow -5\ mm \rightarrow 0\ mm$ with a 0.5 mm step size, respectively. After processing all the test data, the repeated positioning accuracies were 0.168 µm and 0.225 µm, respectively.

Figure 24a,b show the three-cycle rotating test curves in the Rx direction in the range of $0^\circ \rightarrow 0.01^\circ \rightarrow 0^\circ \rightarrow -0.01^\circ \rightarrow 0^\circ$ with a 0.001° step size and $0^\circ \rightarrow 5^\circ \rightarrow 0^\circ \rightarrow -5^\circ \rightarrow 0^\circ$ with a 0.5° step size, and the repeated positioning accuracies were 0.181″and 0.440″, respectively. The repeated positioning accuracy in the Ry direction could be obtained by testing in a similar manner, with results as shown in Table 3.

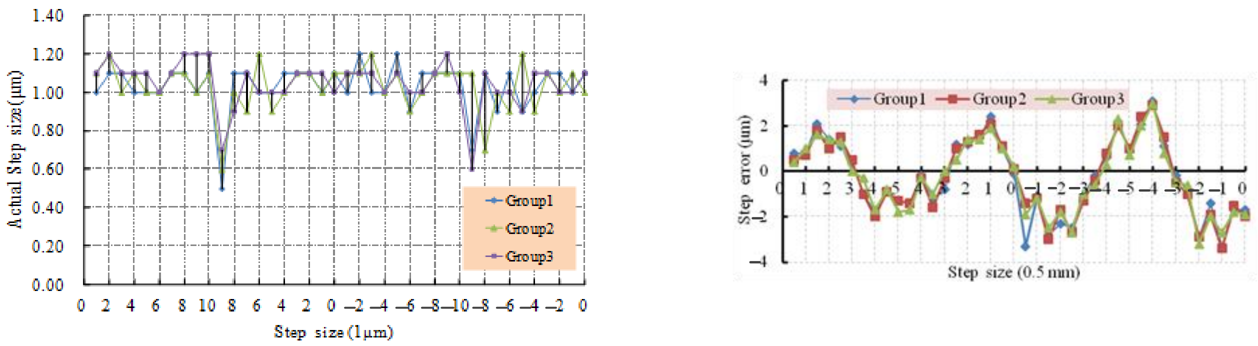

(**a**) (**b**)

Figure 23. Test results for mobile platform translation along *Z*-axis: (**a**) Step size: 1 μm; (**b**) Step size: 0.5 mm.

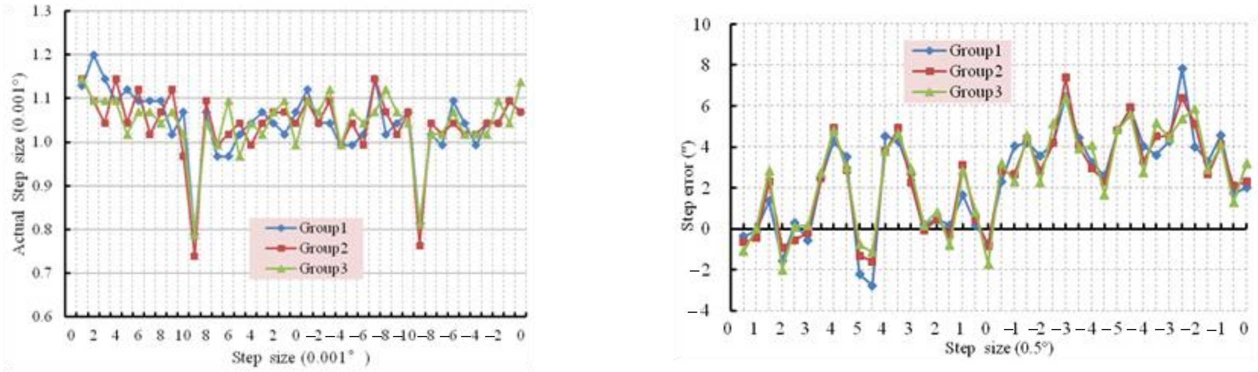

(**a**) (**b**)

Figure 24. Test results for mobile platform rotation along the *X*-axis: (**a**) Step size: 0.001°; (**b**) Step size: 0.5°.

Table 3. Performance characteristics of the parallel platform.

Project Name		Performance
Repeated positioning accuracy	pitch motion (Rotating around *X*-axis)	0.440″ (step size of 0.5°)
		0.181″ (step size of 0.001°)
	yaw motion (Rotating around *Y*-axis)	1.734″ (step size of 0.5°)
		0.108″ (step size of 0.001°)
	focusing motion (Translating around *Z*-axis)	0.225 μm (step size of 0.5 mm)
		0.168 μm (step size of 1 μm)
X-directional static stiffness of the whole platform		7.84 N/μm
Z-directional static stiffness of the whole platform		21.71 N/μm
Natural Frequency (with 30 kg load)		86.25 Hz

4.5. Summary of Platform Performance Indicators

Based on the test results reported above, important performance indices, such as the platform repeated positioning accuracy and the fundamental frequency, are presented in Table 3.

The repeated positioning accuracy of the parallel platform studied in this paper is more excellent overall than that of the parallel platform in [23,24]. The important indices for the platform indicate the rationality and the effectiveness of the platform design. They also show that the configuration of the entire machine, including the layout and the structural forms of the joints and legs, the processing and assembly technology used, and the benchmark system design, play important roles in determining the kinematic accuracy and the stiffness of the entire platform.

5. Conclusions

A 6-*P*-RR-R-RR parallel platform with high lateral and longitudinal stiffness is studied in this paper. The platform is mainly intended for use in the precision adjustment systems for third mirror components in a large-caliber telescope system. In the design process, the large load, high precision, and high stiffness indexes are taken as the design objectives of the platform. The platform has small axial dimension, high bearing capacity, high precision, and high stiffness. Different from the traditional parallel mechanism, the leg drive assembly is installed on the base platform surface at an inclination angle of 30°, with low configuration height, which greatly reduces the height of the whole machine, improves the lateral stiffness of the whole machine, and increases the movement stroke of the driving inclined block. The parallel platform adopts offset RR joint with non-intersecting rotating shafts to replace the traditional universal joint, which has a larger bearing capacity and is easier to process and adjust, reducing the risk of interference between joints and other parts in the process of rotation. In this paper, all possible gaps in the structure are eliminated, and the RR-R-RR series kinematic chain is designed with zero gaps and high stiffness. Each revolute joint in the leg series kinematic chain uses a zero-gap dense bead shaft composed of two columns of high-precision large-diameter steel balls rather than the traditional bearing supported rotation joint and is appropriately pre-tightened, thus eliminating the movement gap while increasing the stiffness of the leg kinematic chain. The joint and leg installation datum is designed to improve the assembly precision of the kinematic chain. Different from the common 6-SPS, 6-UCU, and 6-UPS configurations, due to the additional variables introduced by the offset hinge, the traditional kinematic modeling method of parallel mechanism cannot be used to establish the kinematic model of the 6-*P*-RR-R-RR parallel platform. The D-H parameter method is successfully used to establish the complex kinematics mathematical model of the parallel platform, and the correctness of the model is verified via co-simulations. The introduction of the D-H parameter method provides a new solution for the kinematic analysis of complex parallel mechanisms. It lays a foundation for the subsequent analysis of velocity, acceleration, and dynamics. A parallel platform test system that mainly consisted of a test fixture, a simulated load, the grating length gauges, and the display instruments was constructed and motion performance testing was carried out. The static and dynamic stiffness of the platform were then tested to verify the rationality of the proposed design.

Author Contributions: Conceptualization, H.H. and Z.X.; methodology, H.H., Y.Z., and C.H.; software, A.L.; validation, H.H., Y.Z., and H.Z.; formal analysis, H.H.; investigation, Y.Z.; data curation, Y.Z. and H.Z.; writing—original draft preparation, H.H. and Y.Z.; writing—review and editing, Y.Z.; supervision, Z.X.; project administration, H.H. and Z.X.; funding acquisition, H.H. and C.H. All authors have read and agreed to the published version of the manuscript.

Funding: This research was funded by the National Natural Science Foundation of China, grant number 52005478, and the Jilin Scientific and Technological Development Program, grant number 20200404204YY.

Institutional Review Board Statement: Not applicable.

Informed Consent Statement: Not applicable.

Data Availability Statement: The data presented in this study are available on request form the corresponding author.

Conflicts of Interest: The authors declare no conflict of interest.

References

1. Sreenivasan, S.V.; Waldron, K.J.; Nanua, P. Closed-form direct displacement analysis of a 6-6 Stewart platform. *Mech. Mach. Theory* **1994**, *29*, 855–864. [CrossRef]
2. Wu, P.; Xiong, H.; Kong, J. Dynamic analysis of 6-SPS parallel mechanism. *Int. J. Mech. Mater. Des.* **2012**, *8*, 121–128. [CrossRef]
3. Liu, G.; Qu, Z.; Liu, X.; Han, J. Singularity analysis and detection of 6-UCU parallel manipulator. *Robot. Comput. Integr. Manuf.* **2014**, *30*, 172–179. [CrossRef]

4. Liu, Y.; Wu, H.; Yang, Y.; Zou, S.; Zhang, X.; Wang, Y. Symmetrical Workspace of 6-UPS Parallel Robot Using Tilt and Torsion Angles. *Math. Probl. Eng.* **2018**, *2018*, 6412030. [CrossRef]
5. Joumah, A.A.; Albitar, C. Design Optimization of 6-RUS Parallel Manipulator Using Hybrid Algorithm. *Int. J. Inf. Technol. Comput. Sci.* **2018**, *10*, 83–95. [CrossRef]
6. Mirshekari, E.; Ghanbarzadeh, A.; Shirazi, K.H. Structure comparison and optimal design of 6-rus parallel manipulator based on kinematic and dynamic performances. *Lat. Am. J. Solids Struct.* **2016**, *13*, 2414–2438. [CrossRef]
7. Yang, G.; Zhu, R.; Fang, Z.; Chen, C.Y.; Zhang, C. Kinematic Design of a 2R1T Robotic End-Effector with Flexure Joints. *IEEE Access* **2020**, *8*, 57204–57213. [CrossRef]
8. Fang, Y.; Huang, Z. Kinematics of a three-degree-of-freedom in-parallel actuated manipulator mechanism. *Mech. Mach. Theory* **1997**, *32*, 789–796. [CrossRef]
9. Chai, X.; Wang, M.; Xu, L.; Ye, W. Dynamic modeling and analysis of a 2PRU-UPR parallel robot based on screw theory. *IEEE Access* **2020**, *8*, 78868–78878. [CrossRef]
10. Huang, Z.; Fang, Y.F. Kinematic characteristics analysis of 3 DOF in-parallel actuated pyramid mechanisms. *Mech. Mach. Theory* **1996**, *31*, 1009–1018. [CrossRef]
11. Han, C.; Kim, J.; Kim, J.; Park, F.C. Kinematic sensitivity analysis of the 3-UPU parallel mechanism. *Mech. Mach. Theory* **2002**, *37*, 787–798. [CrossRef]
12. Richard, P.L.; Gosselin, C.M.; Kong, X. Kinematic analysis and prototyping of a partially decoupled 4-DOF 3T1R parallel manipulator. *J. Mech. Des. Trans. ASME* **2007**, *129*, 611–616. [CrossRef]
13. Zhang, C.; Li, B.; Zhao, X.; Li, Y. Kinematics analysis of a four degree-of-freedom parallel manipulator. In Proceedings of the 2017 IEEE International Conference on Robotics and Biomimetics (ROBIO), Macau, Macao, 5–8 December 2017; Institute of Electrical and Electronics Engineers (IEEE): New York, NY, USA, 2018; pp. 1731–1736. [CrossRef]
14. Li, Q.; Huang, Z.; Hervé, J.M. Type synthesis of 3R2T 5-DOF parallel mechanisms using the lie group of displacements. *IEEE Trans. Robot. Autom.* **2004**, *20*, 173–180. [CrossRef]
15. Lu, Y. Simulation of machining 3D free-form surface in normal direction using 6-SSP and 4SPS + UPU parallel machine tools. *Int. J. Adv. Manuf. Technol.* **2007**, *33*, 1180–1188. [CrossRef]
16. Gough, V.E. Contribution to discussion of papers on research in automobile stability, control and tyre performance. *Proc. Automot. Div. Inst. Mech. Eng.* **1956**, *171*, 392–395.
17. Stewart, D. A platform with six degrees of freedom. *Proc. Inst. Mech. Eng.* **1965**, *180*, 371–386. [CrossRef]
18. Shiga, Y.; Tanaka, Y.; Goto, H.; Takeda, H. Design of a six degree-of-freedom tripod parallel mechanism for flight simulators. *Int. J. Autom. Technol.* **2011**, *5*, 715–721. [CrossRef]
19. Zhang, D.; Lang, S.Y.T. Stiffness modeling for a class of reconfigurable PKMs with three to five degrees of freedom. *J. Manuf. Syst.* **2004**, *23*, 316–327. [CrossRef]
20. Huang, T.; Li, Z.; Li, M.; Chetwynd, D.G.; Gosselin, C.M. Conceptual design and dimensional synthesis of a novel 2-DOF translational parallel robot for pick-and-place operations. *J. Mech. Des. Trans. ASME* **2004**, *126*, 449–455. [CrossRef]
21. Yang, J.; Xu, Z.; Wu, Q.; Zhu, M.; He, S.; Qin, C. Dynamic modeling and control of a 6-DOF micro-vibration simulator. *Mech. Mach. Theory.* **2016**, *104*, 350–369. [CrossRef]
22. Yang, J.; Xu, Z.; Wu, Q.; Li, Y.; Chen, L.; Gu, Y. Design of six dimensional vibration isolation system for space optical payload. *Opt. Precis. Eng.* **2015**, *23*, 1347–1357. [CrossRef]
23. Geijo, E.M.; Casalta, J.M.; Canchado, M.; Andrés, M.S.; Brú, R.; Garcia, H.; Tomás, A.; Zago, L.; Jeffers, P. VISTA secondary mirror drive performance and test results. In *Optomechanical Technologies for Astronomy*; International Society for Optics and Photonics: Bellingham, WA, USA, 2006; Volume 6273, p. 627338. [CrossRef]
24. Schipani, P.; D'Orsi, S.; Fierro, D.; Marty, L.; Perrotta, F.; Arcidiacono, C. Performance of the VST secondary mirror support system. In *Modern Technologies in Space-and Ground-based Telescopes and Instrumentation*; International Society for Optics and Photonics: Bellingham, WA, USA, 2010; Volume 7739, p. 773932. [CrossRef]
25. Shoham, M.; Burman, M.; Zehavi, E.; Joskowicz, L.; Batkilin, E.; Kunicher, Y. Bone-Mounted Miniature Robot for Surgical Procedures: Concept and Clinical Applications. *IEEE Trans. Robot. Autom.* **2003**, *19*, 893–901. [CrossRef]
26. Nakano, T.; Sugita, N.; Ueta, T.; Tamaki, Y.; Mitsuishi, M. A parallel robot to assist vitreoretinal surgery. *Int. J. Comput. Assist. Radiol. Surg.* **2009**, *4*, 517–526. [CrossRef] [PubMed]
27. Petrescu, R.V.V.; Aversa, R.; Apicella, A.; Kozaitis, S.; Abu-Lebdeh, T.; Petrescu, F.I.T. Inverse Kinematics of a Stewart Platform. *J. Mechatron. Robot.* **2018**, *2*, 45–59. [CrossRef]
28. Liu, G.; Zheng, S.; Ogbobe, P.; Han, J. Inverse kinematic and dynamic analyses of the 6-UCU parallel manipulator. *Appl. Mech. Mater.* **2012**, *127*, 172–180. [CrossRef]
29. Khalil, W.; Guegan, S. Inverse and Direct Dynamic Modeling of Gough-Stewart Robots. *IEEE Trans. Robot.* **2004**, *20*, 754–761. [CrossRef]
30. Ji, P.; Wu, H. Kinematics analysis of an offset 3-UPU translational parallel robotic manipulator. *Robot. Auton. Syst.* **2003**, *42*, 117–123. [CrossRef]
31. Hu, B.; Lu, Y. Analyses of kinematics, statics, and workspace of a 3-RRPRR parallel manipulator and its three isomeric mechanisms. *Proc. Inst. Mech. Eng. Part C J. Mech. Eng. Sci.* **2008**, *222*, 1829–1837. [CrossRef]

32. Dalvand, M.M.; Shirinzadeh, B. Forward kinematics analysis of offset 6-RRCRR parallel manipulators. *Proc. Inst. Mech. Eng. Part C J. Mech. Eng. Sci.* **2011**, *225*, 3011–3018. [CrossRef]
33. Dalvand, M.; Shirinzadeh, B. Kinematics Analysis of 6-DOF Parallel Micro-Manipulators with Offset U-Joints: A Case Study. *Int. J. Intell. Mechatron. Robot.* **2012**, *2*, 28–40. [CrossRef]
34. Dalvand, M.; Shirinzadeh, B.; Nahavandi, S. Inverse kinematics analysis of 6-RRCRR parallel manipulators. In Proceedings of the IEEE/ASME International Conference on Advanced Intelligent Mechatronics, Wollongong, Australia, 9–12 July 2013; pp. 644–648. [CrossRef]
35. Großmann, K.; Kauschinger, B. Eccentric universal joints for parallel kinematic machine tools: Variants and kinematic transformations. *Prod. Eng.* **2012**, *6*, 521–529. [CrossRef]
36. Gloess, R.; Lula, B. Challenges of extreme load hexapod design and modularization for large ground-based telescopes. In *Modern Technologies in Space-and Ground-Based Telescopes and Instrumentation*; International Society for Optics and Photonics: Bellingham, WA, USA, 2010; Volume 7739, p. 77391U. [CrossRef]